

**Tuning Defects in the MoS<sub>2</sub>/Reduced Graphene Oxide 2D Hybrid Materials for Optimizing Battery Performance**

Journal:	<i>Sustainable Energy &amp; Fuels</i>
Manuscript ID	SE-ART-05-2021-000729.R1
Article Type:	Paper
Date Submitted by the Author:	26-Jun-2021
Complete List of Authors:	Muthukumar, kamalambika; Kansas State University, Chemistry Li, Jun; Kansas State University, Department of Chemistry Leban II, Levon; Kansas State University Sekar, Archana; Kansas State University Elangovan, Ayyappan; Kansas State University College of Arts and Sciences, Chemistry; Sarkar, Nandini; Kansas State University, Department of Chemistry

## **Tuning Defects in the MoS<sub>2</sub>/Reduced Graphene Oxide 2D Hybrid Materials for Optimizing Battery Performance**

Kamalambika Muthukumar, Levon Leban II, Archana Sekar, Ayyappan Elangovan, Nandini Sarkar, and Jun Li\*

Department of Chemistry, Kansas State University, Manhattan, Kansas, 66506, USA.

### **Corresponding Author:**

Prof. Jun Li,  
Department of chemistry,  
Kansas State University  
Manhattan, Kansas 66506, USA  
Email: junli@ksu.edu

**Abstract:**

This study reports the preparation of a set of hybrid materials consisting of Molybdenum disulfide ( $\text{MoS}_2$ ) nanopatches on reduced graphene oxide (rGO) nanosheets by applying the microwave specific heating of graphene oxide and molecular molybdenum precursors followed by a thermal annealing in 3%  $\text{H}_2$  and 97% Ar. The microwave process converts graphene oxide to ordered rGO nanosheets that are sandwiched between uniform thin layers of amorphous Molybdenum trisulfide ( $\text{MoS}_3$ ). The subsequent thermal annealing converts the intermediate layers into  $\text{MoS}_2$  nanopatches with two-dimensional layered structures whose defect density is tunable by controlling the annealing temperature at 250, 325 and 600 °C, respectively. All three  $\text{MoS}_2/\text{rGO}$  samples and the  $\text{MoS}_3/\text{rGO}$  intermediate after the microwave step show a high Li-ion intercalation capacity in initial 10 cycles (over 519 mAh  $\text{g}_{\text{MoS}_x}^{-1}$ ,  $\sim 3.1 \text{ Li}^+$  ions per  $\text{MoS}_2$ ) which is attributed to the small  $\text{MoS}_2$  nanopatches in the  $\text{MoS}_2/\text{rGO}$  hybrids while the effect of further S-rich defects is insignificant. In contrast, the Zn-ion storage properties strongly depend on the defects in the  $\text{MoS}_2$  nanopatches. The highly defective  $\text{MoS}_2/\text{rGO}$  hybrid prepared by annealing at 250 °C shows the highest initial Zn-ion storage capacity ( $\sim 300 \text{ mAh g}_{\text{MoS}_x}^{-1}$ ) and close to 100% coulombic efficiency, which is dominated by pseudocapacitive surface reactions at the edges or defects in the  $\text{MoS}_2$  nanopatches. The fast fading in initial cycles can be mitigated by applying higher charge/discharge currents or extended cycles. This study validates that defect engineering is critical in improving Zn-ion storage.

**Keywords:**

Reduced graphene oxide,  $\text{MoS}_2/\text{rGO}$  hybrid, defect engineering, Mo vacancies, Zinc-ion batteries

**Introduction:**

Electrical energy storage (EES) has become an essential part of the modern world. The rising energy consumption and the global demand for clean energy are driving the development of EES systems that can be integrated with the existing energy systems. At present, an unmet demand is the large-scale EES systems<sup>1, 2</sup> to support the electrical grids and intermittent renewable energy techniques. Many EES systems such as Nickel-cadmium, Ni-MH, Lead acid batteries and Li-ion batteries (LIBs) have been extensively studied in the past years for this application. LIB is the leading technology due to its high specific capacity and decent lifetime. However, LIBs are limited by the high cost, low materials abundance, usage of flammable and toxic electrolytes, and environmental or safety issues. Multivalent metal-ion batteries such as Mg-ion batteries (MIBs) and Zn-ion batteries (ZIBs) have been identified as alternatives for the large-scale EES systems due to their divalent nature, higher volumetric capacity, high natural abundance and superior safety features<sup>2-5</sup>. The aqueous ZIBs are particularly attractive due to the environmental compatibility and low cost<sup>6</sup>. Many materials, including manganese oxides<sup>6-8</sup>, vanadium oxides<sup>9, 10</sup> and metal organic frameworks (such as Prussian blue analogues)<sup>11, 12</sup>, have been explored as the cathode materials for ZIBs. Most of these materials are based on intercalation of the multivalent ions in the host materials, which exhibits strong interactions with the host lattice and largely varied results. For example, the NASICON-structured  $\text{Na}_3\text{V}_2(\text{PO}_4)_3$  cathode showed a moderate capacity of  $97 \text{ mAh g}^{-1}$  at  $0.5 \text{ C}$  and was able to retain 74% of the capacity after 100 cycles<sup>13</sup> and the  $\text{MoO}_2/\text{Mo}_2\text{N}$  heterostructured nanobelts showed a similar capacity of  $113 \text{ mAh g}^{-1}$  at  $1 \text{ A g}^{-1}$  for 1000 cycles<sup>14</sup>. In contrast, the layered  $\text{H}_2\text{V}_3\text{O}_8$  nanowire cathode exhibited a much higher capacity of  $423.8 \text{ mAh g}^{-1}$  at  $0.1 \text{ A g}^{-1}$  with 84.3% capacity retention after 1000 cycles<sup>15</sup>. Recently, it has been proposed that the proton intercalation may be the dominant reaction in these materials instead of intercalation by the divalent metal ions<sup>4, 5</sup>.

Transition metal dichalcogenides such as MoS<sub>2</sub> have caught attention as a potential host for both monovalent and divalent ions due to their unique two-dimensional (2D) layered structure and the high theoretical capacity for Li-ion storage (up to 669 mAh g<sup>-1</sup>)<sup>16-19</sup>. The MoS<sub>2</sub> structure consists of a layer of molybdenum atoms covalently bonded between two layers of sulfur atoms. The triatomic layers of MoS<sub>2</sub> are linked by weak van der Waals forces<sup>20,21</sup> similar to graphene, which can effectively accommodate the volume expansion to facilitate reversible intercalation/deintercalation of metal ions. The sulfur atoms in MoS<sub>2</sub> have higher softness than oxygen atoms in metal oxides, which further improves the reversibility of intercalation/deintercalation of divalent metal ions<sup>4, 5</sup>. Despite the high theoretical capacity, MoS<sub>2</sub> suffers from the low electrical conductivity and pulverization of the structure after a few cycles. The specific capacity for zinc-ion storage in high-quality MoS<sub>2</sub><sup>22</sup> was found to be only a few mAh g<sup>-1</sup><sup>22</sup>. These problems can be mitigated by modifying the structure through (1) increasing the interlayer spacing<sup>10, 23</sup>, (2) introducing active defects in the MoS<sub>2</sub> structure to enhance Zn<sup>2+</sup> ion adsorption<sup>22</sup>, and (3) forming a hybrid structure with carbonaceous materials to improve the electrical conductivity, mechanical strength and structural stability of MoS<sub>2</sub> layers<sup>24, 25</sup>. Among which, defect engineering has been recently explored as an effective approach to enhance the specific capacity of MoS<sub>2</sub> towards the storage of monovalent and divalent ions including Li<sup>+</sup>, Na<sup>+</sup>, Zn<sup>2+</sup> ions<sup>22, 26, 27</sup>. The defect-rich MoS<sub>2</sub> with sulfur vacancies was found to be effective in boosting the zinc-ion storage to 88.6 mAh g<sup>-1</sup> at 1 A g<sup>-1</sup> which was stable over 1,000 cycles when compared to pristine MoS<sub>2</sub><sup>22</sup>. So far, the physical and chemical exfoliation techniques tend to form sulfur defects rather than molybdenum defects. Despite the high formation energy of 6.93 eV, Mo vacancies present many advantages including increased active sites, low diffusion energy, improved electrical conductivity and enhanced charge transfer ability. The Mo vacancies in the structure is reported to accelerate the charge transfer process and has strong binding affinity for the intercalating cations<sup>27</sup>. However, Mo vacancies

have not been adequately explored for ion storage applications due to the poor stability. The rapid quenching in microwave-assisted synthesis was found to be effective in reducing the mobility of precursors and intermediate species, prevent the agglomeration and preserve the integrity of the defective MoS<sub>2</sub> structure<sup>28</sup>. It could be an efficient method towards the synthesis of hybrid nanomaterial structures with controlled defect engineering<sup>29</sup>. In addition, the rapid heating and cooling processes of microwave-assisted synthesis leads to fast phase transitions and produce nanostructures with small and uniform size distributions, which helps to enhance the ion transport.

In this study, we use a two-step reaction based on the specific microwave heating of the molecular Molybdenum (Mo) precursors and the dispersed graphene oxide (GO) flakes, which is followed by a thermal annealing in 3% H<sub>2</sub> and 97% Ar. Compared to the conventional hydrothermal process, the microwave-assisted synthesis significantly reduces reaction time<sup>30</sup> by directly activating the polar molecules and heating the reaction system uniformly<sup>31</sup>. The high dissipation factor (or  $\tan \delta$  value) of the Mo precursor and GO is utilized to generate specific microwave heating to effectively convert GO into reduced graphene oxide (rGO) and induce the growth of MoS<sub>3</sub> intermediate material over the rGO template. By applying thermal annealing, the MoS<sub>3</sub> intermediate is converted into MoS<sub>2</sub> nanopatches anchored on the large monocrystalline rGO nanosheets. The 2D layered structure of MoS<sub>2</sub> and rGO enables them to remain stacked as a stable hybrid material. The defect density in the MoS<sub>2</sub> nanopatches is tuned from the highly defective form with abundant S-rich (or Mo-deficient) defects at the annealing temperature of 250 °C to much less defective form at 600 °C. The unique structure and composition of these hybrid materials are systematically characterized and their energy storage properties as the LIB anodes and ZIB cathodes have been assessed. The results reveal that the defects in MoS<sub>2</sub>/rGO hybrids are insignificant for Li-ion storage based on the interlayer intercalation but have a dramatic effect on Zn-ion storage. The highly defective MoS<sub>2</sub>/rGO

hybrid works the best for Zn-ion storage which is dominated by pseudocapacitive surface reactions. These results provide new insights in developing ZIB cathode materials.

### **Experimental:**

#### **▪ Materials:**

The precursors including Ammonium tetrathiomolybdate (ATM) and single-layer GO powder were purchased from Sigma Aldrich (St. Louis, MO) and ACS material LLC (Pasadena, CA), respectively. The CR2025 and CR2032 coin cell components were purchased from MTI corporation (Richmond, CA). The ZIB electrolyte was prepared with commercial zinc sulfate monohydrate from Sigma Aldrich (St. Louis, MO). The LIB electrolyte of Purolyte A4 series with 1.0 M LiPF<sub>6</sub> was purchased from Novolyte Battery Materials Co., Ltd. (Suzhou, Jiangsu, China).

#### **▪ Preparation of MoS<sub>2</sub>/rGO hybrid:**

To synthesize MoS<sub>2</sub>/rGO, 15.0 mM ATM and 5.0 mg GO were dispersed in 6.0 ml tetrahydrofuran (THF) mixed with 1.0 ml distilled water. This mixture was ultrasonicated for about 20 minutes to obtain a homogenous suspension, which was then transferred to a 10 ml Pyrex glass microwave tube and put into an automated microwave system (Discover SP, CEM Corp., Matthews, NC) to irradiate with a microwave power of 300 W under the dynamic mode. It took approximately 7 minutes for the temperature to ramp up to the setting of 170°C and then the system was held at this temperature for 10 min. During the reaction, the pressure went up to ~21 bar depending on the reaction conditions. After the reaction is over, the system was vented with compressed air and cooled down to the room temperature. The product was collected and centrifuged at 2000 rpm for about 15 min. The solid precipitate was collected and dried on a hotplate in the air at ~80 °C overnight. The dried material was further annealed in 3% H<sub>2</sub> and 97% Ar at 250°C, 325°C, and 600 °C, respectively. The corresponding samples

were denoted as MoS<sub>2</sub>/rGO-250, MoS<sub>2</sub>/rGO-325 and MoS<sub>2</sub>/rGO-600, respectively. The control sample of bare rGO was synthesized following the same procedure as the MoS<sub>2</sub>/rGO samples except without adding any ATM precursor in the reaction mixture.

▪ **Material Characterization:**

The Raman spectroscopy analysis was performed with a DXR<sup>TM</sup> Raman microscope (Thermo fisher Scientific, Madison, WI) with a 532 nm laser at the power of 10 mW, under a 10X objective lens with a slit width of 50 μm. The X-ray diffraction (XRD) study was done with a D8 Advance diffractometer (Bruker Corporation, Karlsruhe, Germany) with a Cu Kα radiation of wavelength 0.15418 nm and a slit width of 2 mm. The obtained XRD spectra of MoS<sub>2</sub>/rGO materials were further smoothed with origin pro software using a 5-point adjacent average filter. The surface composition and chemical environment of MoS<sub>2</sub>/rGO hybrids were analyzed using a PHI 5000 Versa XPS system (Chanhassen, MN) with a monochromatized Al Kα source (1486.7 eV). The transmission electron microscopy (TEM) images were obtained using Philips CM 100 with a tungsten source and a high tension of 100 kV. The field emission scanning electron microscopy (FESEM) images were obtained using a Topcon/ISI/ABT DS 130F FESEM microscope (Akashi Beam Technology Corporation, Tokyo, Japan). Thermogravimetric analysis (TGA) were carried out with TGA Q50 system (TA instruments - Waters LLC, New Castle, DC) from the room temperature to 600 °C in the air. Elemental analysis results (%C, %H, %N, %S) presented in this work were acquired using a PE 2100 Series II combustion analyzer (Perkin Elmer Inc., Waltham, MA). The combustion tube packing was supplied with the instrument and consisted of the following components: copper oxide wires and electrolytic copper was used for CHNS reduction and the oxygen reduction tube was packed with nickel plated carbon and quartz turning. The compounds were sampled using pressed tin capsules for CHNS Analysis and silver capsules for O analysis. 2,5-Bis(5-tert-butyl-benzoxazol-2-yl) thiophene was used as calibration standard for all the samples

unless notified otherwise in the discussion. The combustion and reduction temperature were 975°C for CHNS analysis. All the standards and reagents were purchased from Perkin Elmer or Elemental America's Inc. The precision and accuracy of the results were estimated to be as low as +/- 0.3%. Vanadium pentoxide was used as combustion aid for sulfur analysis.

▪ **Electrochemical Characterization:**

A slurry was prepared by mixing the active material (i.e. MoS<sub>x</sub>/rGO), carbon additive (Super-P, Alfa Aesar Co. Ltd., Massachusetts, USA) and a poly(vinylidene fluoride-co-hexafluoropropylene) (PVDF, Sigma Aldrich Co., St. Louis, MO) binder at the weight ratio of 8:1:1 with approximately 150 μL of N-methyl-2-pyrrolidone (NMP, Sigma Aldrich, St. Louis, MO) as the solvent. The homogenous slurry was then brush-coated onto a 0.10 mm thick titanium disk (MTI Corporation, Richmond, CA) with a diameter of 15 mm for ZIB half-cell tests. The coated electrodes were vacuum dried at 110°C overnight and used as the cathode in ZIBs. A Zn disk (Sigma Aldrich, St. Louis, Mo) of 0.25 mm thickness and 15 mm diameter was used as the anode. Commercially purchased glass fiber disk (El-Cell, Hamburg, Germany) of 18 mm diameter and 0.65 mm thickness was used as the separator. A 0.3 mm thick stainless-steel wave spring and a 0.5 mm thick stainless spacer were placed behind the cathode to protect the electrode structure. The electrode and separator stacks were assembled into stainless steel coin cells (CR 2025, MTI Corporation, Richmond, CA) in the ambient atmosphere with 2.0 M ZnSO<sub>4</sub> aqueous solution as the electrolyte. Electrochemical characterization of the cells was carried out in the cell voltage window of 0.25 - 1.3 V in ZIB half-cell tests.

The MoS<sub>2</sub>/rGO material was also tested as the LIB anode in a half-cell in stainless steel coin cells (CR-2032, MTI Corporation, Richmond, CA). The MoS<sub>2</sub>/rGO slurry was prepared like ZIB cathode described above. The prepared MoS<sub>2</sub> slurry was brush-coated on a copper disk of 0.10 mm in thickness and 15 mm in diameter. The electrolyte used in LIB tests was 1.0

M LiPF<sub>6</sub> in a mixture of 1:1:1 (v/v/v) ethylene carbonate (EC), ethyl methyl carbonate (EMC) and dimethyl carbonate (DMC) with 2% vinylene carbonate additive. All LIB cells were assembled in an argon-filled LabStar 50 stainless steel glovebox (MBraun, Garching, Germany) in a controlled atmosphere of < 0.5 ppm O<sub>2</sub> and < 0.5 ppm H<sub>2</sub>O. The tests were carried out in the cell voltage window of 0.50 - 3.0 V. All battery tests were done with a BTS 4000 5V 50 mA Battery Tester (Neware, Shenzhen, China) and the Cyclic Voltammetry (CV) tests were performed using CHI 440A (CH Instruments Inc., Austin, TX).

The galvanostatic charge/discharge curves were measured at constant cell current at preset values. However, the mass of the coated material varied between 1.0 and 2.0 mg on each electrode, which can be determined by measuring the weight of bare Ti or Cu disks and those after coating and drying the active materials. In order to compare electrode performance at similar current densities, the cell currents were converted into the current densities in some figures. The control rGOs were measured in the same way for both Li-ion and Zn-ion half cells by replacing the active materials with corresponding rGOs.

## Results and Discussion

### ▪ Synthesis design:

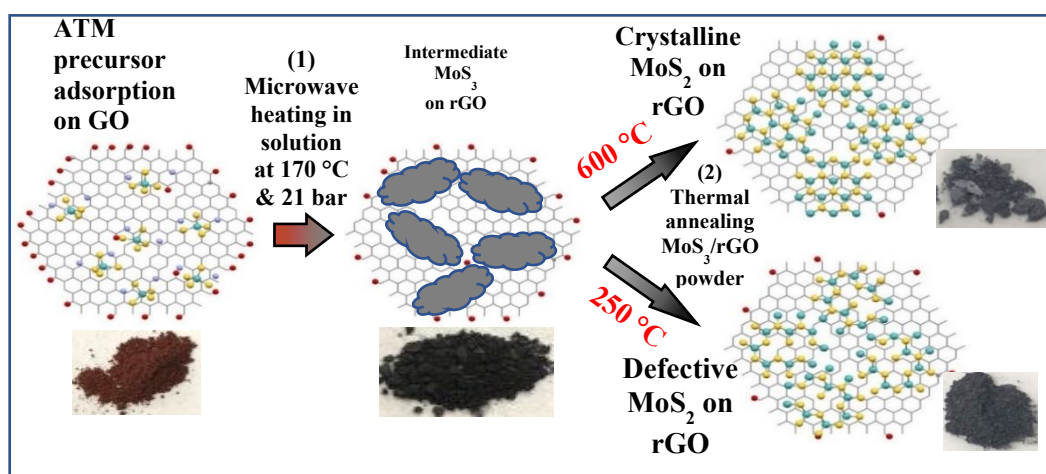
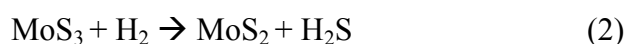


**Figure 1.** Schematic illustration of the two-step synthesis of MoS<sub>2</sub>/rGO hybrid materials by microwave-heating of ATM and GO precursors in THF followed by thermal annealing the intermediate MoS<sub>3</sub>/rGO powder at varied temperature in 3%H<sub>2</sub>/97%Ar in a tube furnace.

Microwave irradiation technique is reported to be a facile technique for the rapid synthesis of hybrid materials. A two-step method has been employed here to synthesize the MoS<sub>2</sub>/rGO hybrid materials with tunable defect densities. As shown in Figure 1, in the first step, the 10 min specific heating by microwave irradiation is used to convert the ammonium tetra thiomolybdate (ATM) and GO precursors in tetrahydrofuran (THF) solution. At the reaction conditions of 170 °C and ~21 bar, a large portion of the adsorbed ATM molecules are converted into solid MoS<sub>3</sub> nanoparticles while the GO precursors are converted into reduced graphene oxide (rGO) nanosheets, forming the intermediate MoS<sub>3</sub>/rGO hybrid material<sup>32</sup> via the following reaction:



The deep red-brown colored ATM/GO precursors are converted into the dark brown MoS<sub>3</sub>/rGO intermediate in this process. As will be discussed in later sections, the MoS<sub>3</sub> intermediate has an amorphous chain structure with a composition of Mo<sup>4+</sup>(S<sup>2-</sup>)(S<sub>2</sub><sup>2-</sup>). The Mo is reduced from Mo<sup>6+</sup> to Mo<sup>4+</sup> while some S<sup>2-</sup> is oxidized into S<sub>2</sub><sup>2-</sup>. In the 2<sup>nd</sup> step, the intermediate MoS<sub>3</sub>/rGO powder is further converted to black/grey MoS<sub>2</sub>/rGO hybrids by thermal reduction of S<sub>2</sub><sup>2-</sup> into S<sup>2-</sup> at 250 to 600 °C in a mixed gas of 3% H<sub>2</sub> and 97% Ar in a quartz tube furnace, following the reaction<sup>33</sup>:



The obtained MoS<sub>2</sub> varies from crystalline materials at high annealing temperature (up to 600 °C) to defective materials at lower annealing temperature (down to 250 °C). At the meantime, the quality of rGO is further improved by the thermal annealing.

It is noteworthy that the microwave-assisted technique is not only used to synthesize the high-quality 2D hybrid materials<sup>30</sup> but also help to control the defects in the MoS<sub>2</sub> structure in this structure. Comparing to the conventional hydrothermal process, the microwave-assisted

synthesis reduces the reaction time by more than 70 times, i.e. from more than 12 hours to ~10 minutes<sup>30</sup>. The microwave energy directly activates the molecules that possess large dipole moments or ionic groups and thus heats the reaction system rapidly and uniformly<sup>31</sup>. A material's ability to absorb the microwave radiation and convert the energy into heat is determined by its dissipation factor or the  $\tan\delta$  value. This allows to rapidly initiate the nucleation and growth of EES materials on carbon templates by specific heating to form hybrid structures with strong interfacial interactions<sup>34, 35</sup>. In this study, the  $\tan\delta$  values are 0.8 - 1 for GO and rGO<sup>36</sup>, 0.16 for MoS<sub>2</sub><sup>37</sup> and 0.042 for THF solvent<sup>38</sup>, respectively. Thus, the conversion of ATM into MoS<sub>3</sub> mostly occurs on the hot GO/rGO surface, forming an amorphous MoS<sub>3</sub> layer on the rGO template. As shown in Figure 1 and supported by the characterization results below, the adsorbed MoS<sub>3</sub> intermediate is subsequently converted into randomly oriented small 2D MoS<sub>2</sub> nanopatches lying flatly on the planar rGO nanosheets.

▪ **Structure Characterization:**

Figure 2(a) shows the powder XRD spectra of the MoS<sub>2</sub>/rGO hybrids after annealing in 3%H<sub>2</sub> and 97%Ar at 600, 325 and 250 °C, respectively, denoted as MoS<sub>2</sub>/rGO-600, MoS<sub>2</sub>/rGO-325 and MoS<sub>2</sub>/rGO-250. The XRD spectrum of MoS<sub>2</sub>/rGO-600 consists of four broad peaks around  $2\theta$  angle of 13.4°, 32.6°, 39.5° and 58.3°, which can be attributed to the (002), (100), (103) and (110) diffraction of MoS<sub>2</sub> crystallites. These are consistent with the hexagonal 2H-MoS<sub>2</sub> structure as shown by the standard spectrum of JCPDS card No. 37-1492 and the spectrum of the commercial bulk MoS<sub>2</sub> powders. The (100) peak shows an asymmetric shape, likely due to overlap with the weaker (101) peak at  $2\theta = 33.5^\circ$ . The  $2\theta$  angle of (002) peak is notably shifted from 14.38° in the standard to 13.44°, indicating a small increase of interlayer distance from 0.615 nm to 0.66 nm likely due to the presence of defects in the MoS<sub>2</sub>

layers. The (002) peak of MoS<sub>2</sub>/rGO-600 is quite broad with a full width at the half-maximum (FWHM) of  $\Delta 2\theta = \sim 5^\circ$ . Following the Scherrer equation

$$\tau = \frac{K\lambda}{(\Delta 2\theta) \cos\theta} \quad (3)$$

where the shape factor is assumed to be  $K = 0.9$  and the X-ray wavelength is  $\lambda = 0.154$  nm, the mean size of the ordered (crystalline) domains normal to the MoS<sub>2</sub> layer is estimated as  $\tau = \sim 1.6$  nm. This value corresponds to an ordered stack of only 3 or 4 MoS<sub>2</sub> layers, which is expected to be smaller than the physical grain thickness. Associated with this, the higher order diffraction peaks, such as (006) and (008) peaks shown in bulk MoS<sub>2</sub> powder, are not observed in MoS<sub>2</sub>/rGO-600 hybrid. The FWHM of (100) peak is  $\Delta 2\theta = \sim 1.84^\circ$ , giving the ordered in-plane domain size of  $\tau = \sim 4.5$  nm, which is three times of the ordered stack thickness but is still very small. Thus, they are referred to as “nanopatches”. In addition, a broad peak at  $2\theta = 8.1^\circ$  is attributed to (002) diffraction from rGO layers. The d-spacing is calculated to be  $\sim 0.55$  nm, which is larger than 0.34 nm of the interlayer spacing in graphite. It is likely that the rGO layers are defective and wrinkled, preventing them from forming compact stacks.

As the annealing temperature decreases, the (002) peak of MoS<sub>2</sub> in the MoS<sub>2</sub>/rGO-325 sample shifts to a lower  $2\theta$  angle and presumably overlaps with the broad (002) peak of rGO, making it difficult to identify. The (100), (103) and (110) diffraction peaks become broader and weaker due to disordering caused by the defects in the MoS<sub>2</sub> layers. With further reduction in the annealing temperature to 250 °C, all the major peaks corresponding to 2H-MoS<sub>2</sub> have disappeared in the sample MoS<sub>2</sub>/rGO-250, suggesting the amorphous nature of the MoS<sub>2</sub> structure. Interestingly, the (002) diffraction from rGO in the MoS<sub>2</sub>/rGO-250 sample still preserves but shifts to lower angle at  $2\theta = 7.1^\circ$ , corresponding to an expanded interlayer spacing of 0.62 nm which is consistent with higher defect density in rGO. The broad rGO

diffraction peaks in all samples indicate that there is little re-stacking of rGO layers, likely due to blocking by the MoS<sub>2</sub> adlayers.

Figure 2(b) shows the full Raman spectra of MoS<sub>2</sub>/rGO-600 which consists of the signature peaks attributed to MoS<sub>2</sub> and rGO. The peaks at 1,341 cm<sup>-1</sup> and 1,582 cm<sup>-1</sup><sup>39, 40</sup> are attributed to the D and G bands originating from the vibrational modes of sp<sup>3</sup> carbon atoms in the defect sites and the in-plane vibration of sp<sup>2</sup>-bonded carbon atom, respectively<sup>41</sup>. The intensity ratio between D band and G band ( $I_D/I_G$ ) is rather large at 1.3, which is higher than 0.9 in the GO precursor (Figure S2), suggesting the high degree of sp<sup>3</sup> defects after the removal of the oxygenated functional groups in the microwave process.<sup>42, 43</sup> This accompanies an

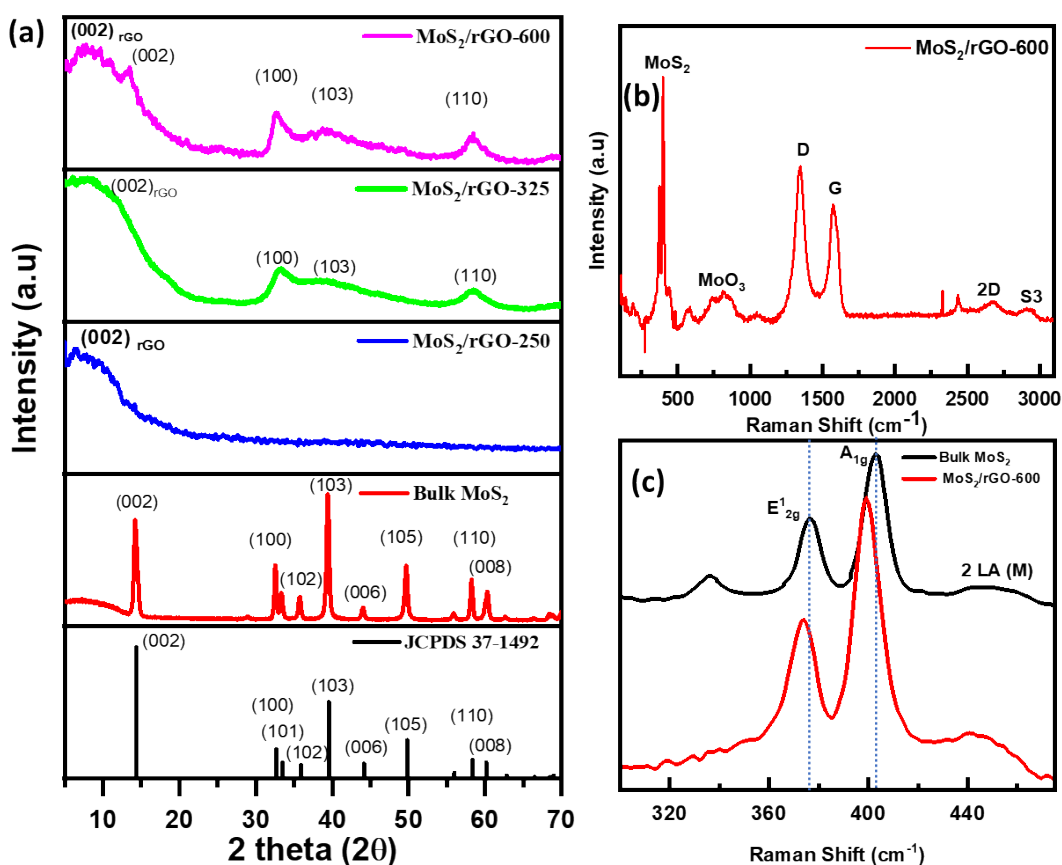


**Figure 2.** (a) Powder XRD spectra of MoS<sub>2</sub>/rGO prepared by annealing at 600 °C (MoS<sub>2</sub>/rGO-600), 325 °C (MoS<sub>2</sub>/rGO-325) and 250 °C (MoS<sub>2</sub>/rGO-250) in comparison to a bulk MoS<sub>2</sub> powder. (b) The full scale and (c) the expanded region of Raman spectra of MoS<sub>2</sub>/rGO-600 and the bulk MoS<sub>2</sub> powder.

increase in the number of smaller graphene domains, which is frequently observed in Raman spectra of rGO<sup>41</sup>. There are also two low-intensity peaks around 2,675 cm<sup>-1</sup> and 2,913 cm<sup>-1</sup>, corresponding to the 2D and S3 bands of rGO. The intensity ratio between S3 and 2D peaks is approximately ~0.40, which is reduced from 1.7 in the GO precursor. The reduced  $I_{S3}/I_{2D}$  value suggests that the defect concentration in the rGO domain was significantly reduced<sup>41</sup>, which is consistent with the XRD results in Figure 2(a). The  $I_D/I_G$  and  $I_{S3}/I_{2D}$  values of all four MoS<sub>x</sub>/rGO hybrids and the GO precursor are shown in Table S1. It is noteworthy that the  $I_{S3}/I_{2D}$  value in all four MoS<sub>x</sub>/rGO hybrids are lower than the GO precursor, confirming the formation of rGO. In this study, some defects in the rGO domains may be preserved which facilitate stronger interaction between the rGO template and the MoS<sub>2</sub> adlayers to form stable hybrid materials.

Figure 2(c) illustrates the three signature bands of MoS<sub>2</sub> at 374.12 cm<sup>-1</sup>, 399.19 cm<sup>-1</sup> and ~445 cm<sup>-1</sup> in MoS<sub>2</sub>/rGO-600, which are attributed to E<sub>2g</sub><sup>1</sup>, A<sub>1g</sub> and 2 LA(M) modes, respectively<sup>24, 44</sup>. The E<sub>2g</sub><sup>1</sup> band arises from the in-plane vibration of the two S atoms with respect to the Mo atom and the A<sub>1g</sub> band is due to the out-of-plane vibration of the S atoms<sup>45, 46</sup>. The broader 2 LA(M) band originates from the second order zone edge phonon. It is noteworthy that the E<sub>2g</sub><sup>1</sup> and A<sub>1g</sub> bands of MoS<sub>2</sub>/rGO-600 are red-shifted by ~1.9 and ~3.82 cm<sup>-1</sup> from 376.02 and 403.01 cm<sup>-1</sup>, respectively, of the reference bulk MoS<sub>2</sub> powder. This was reported as an evidence of the formation of MoS<sub>2</sub>/rGO hybrids in which the MoS<sub>2</sub> layer becomes more n-doped<sup>47</sup>. The intensity of A<sub>1g</sub> peak in Figure 2(c) is much higher than that of the E<sub>2g</sub><sup>1</sup> peak. In principle, the ratio of the integrated intensity of E<sub>2g</sub><sup>1</sup> band to A<sub>1g</sub> band may provide the information of number of MoS<sub>2</sub> layers in the stack<sup>48</sup>, but this is difficult for the powder sample since the intensity ratio strongly depends on the orientation of the MoS<sub>2</sub> crystals<sup>46, 49</sup>. However, the difference in the Raman shifts between the A<sub>1g</sub> and E<sub>2g</sub><sup>1</sup> bands can be accurately read as 25.07 cm<sup>-1</sup>, which suggests that the MoS<sub>2</sub> nanopatches deposited on the

rGO template consist of about 5 to 6 layers in average. The Raman spectra of other samples, including  $\text{MoS}_2/\text{rGO}$ -325,  $\text{MoS}_2/\text{rGO}$ -250 and the unannealed  $\text{MoS}_3/\text{rGO}$  intermediate in Figure S1 of the Supporting Information (SI) show very similar features as those of  $\text{MoS}_2/\text{rGO}$ -600 in Figures 2(b) and (c). The ratio of  $\text{MoS}_2$  peaks to the G and D bands of rGO clearly increases with the annealing temperature but the peak positions are unchanged. Also, a weaker peak can be seen at  $816\text{ cm}^{-1}$  in Figures 2(b) and S1, indicating the presence of a small amount of  $\text{MoO}_3$  in all hybrid  $\text{MoS}_2/\text{rGO}$  samples.

The FESEM images in Figures 3(a) and 3(b) show the representative thin-flake morphology of the  $\text{MoS}_2/\text{rGO}$ -600 hybrid material. Uniform  $\text{MoS}_2$  layers have been deposited over the rGO nanosheets varying from  $\sim 5$  to  $30\ \mu\text{m}$  in size. The TEM images in Figures 3(c)

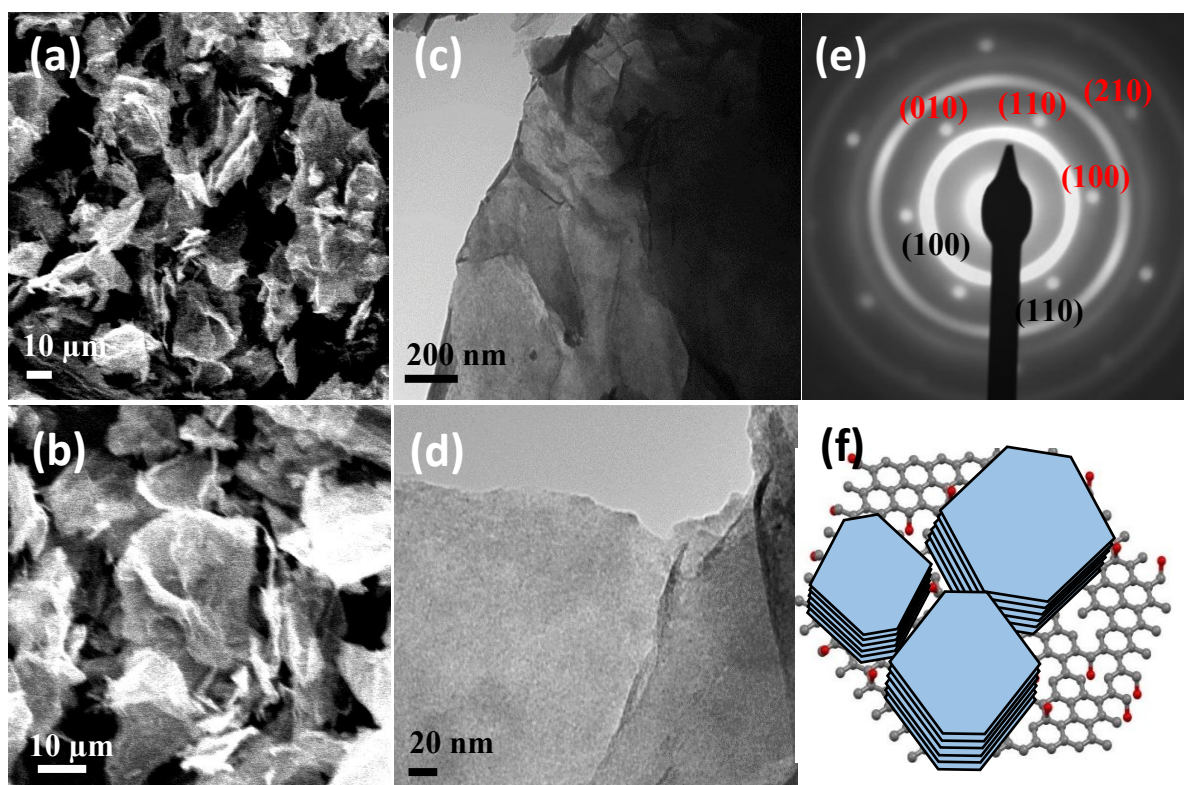


**Figure 3.** Characterization of the  $\text{MoS}_2/\text{rGO}$  hybrid material annealed at  $600\text{ }^\circ\text{C}$  (i.e.,  $\text{MoS}_2/\text{rGO}$ -600) by FESEM at (a) a lower and (b) a higher magnification, by TEM at (c) a lower and (d) a higher magnification, and (e) by the selected area electron diffraction (SAED) from the frame in (d). The red-colored indices at the top portion in panel (e) indicate the isolated hexagonal 2D electron diffraction spots from the monocrystalline rGO nanosheets while the black indices at the bottom indicate the continuous rings of 2D powder electron diffraction from the  $\text{MoS}_2$  adlayers. (f) Schematic illustration of the hybrid structure of  $\text{MoS}_2$  nanopatches with random rotational orientations on the rGO nanosheet.

and 3(d) show the similar flake-like hybrid structure. Due to the small size of MoS<sub>2</sub> nanopatches, it is difficult to clearly see them via TEM imaging. More TEM and FESEM images of the bare rGO nanosheets (synthesized with the same process as MoS<sub>2</sub>/rGO-600 except without adding ATM precursors) and the MoS<sub>3</sub>/rGO intermediate are shown in Figure S3. The bare rGO shows the typical nanoflake structure with small wrinkles due to its softness. After depositing the MoS<sub>3</sub> intermediate material with the microwave synthesis, the adlayers sandwich the rGO nanosheets to form more rigid planar hybrid structures. The morphology of the MoS<sub>3</sub>/rGO intermediate is retained during thermal annealing at the temperature from 250 to 600 °C, as shown by more FESEM images in Figure S4 and TEM images in Figure S5.

The crystallinity of the MoS<sub>2</sub>/rGO hybrid has been further analyzed using Selected Area Electron Diffraction (SAED). The SAED image of MoS<sub>2</sub>/rGO-600 in Figure 3(e) is taken from the area shown in Figure 3(d). It clearly shows two distinct patterns. The dots in the hexagonal lattice are originated from 2D electron diffraction from the monocrystalline rGO nanosheet<sup>50</sup> and the continuous rings are attributed to the randomly oriented polycrystalline 2H-MoS<sub>2</sub> nanopatches on the rGO template. The SAED patterns of MoS<sub>2</sub>/rGO-600, MoS<sub>2</sub>/rGO-325 and MoS<sub>2</sub>/rGO-250 are compared with the un-annealed MoS<sub>3</sub>/rGO intermediate in Figure S6. The sharpness and contrast decrease with the annealing temperature, which indicates the presence of more defects in the MoS<sub>2</sub>/rGO structure at the lower annealing temperature. It is notable that the un-annealed MoS<sub>3</sub>/rGO intermediate shows well-defined hexagonal diffraction spots but no continuous rings, indicating that the microwave irradiation is able to convert GO into monocrystalline rGO nanosheets while the adlayers are dominated by the amorphous MoS<sub>3</sub> intermediate and possibly some ATM precursors.

Figure S7 illustrates how to derive the two dimensional (2D) lattice of MoS<sub>2</sub> in the MoS<sub>2</sub>/rGO hybrid structure from the SAED pattern. At a proper orientation, the incident electron beam is perpendicular to the rGO plane and thus a 2D hexagonal diffraction pattern

can be obtained. The diffraction spots with a six-fold symmetry represent the reciprocal lattice of rGO, which are defined by the instrumental setup and the hexagonal real-space lattice with  $a = b = 2.46 \text{ \AA}$ . The first and second rings are indexed as (100) and (110) diffraction from the hexagonal lattice of  $\text{MoS}_2$ . Using the rGO diffraction spots as the reference, the 2D lattice parameters for  $\text{MoS}_2$  can be derived as  $a = b = 3.16 \text{ \AA}$ , which match well with the structure of bulk 2H- $\text{MoS}_2$  crystals. Interestingly, the SAED pattern also indicates that the  $\text{MoS}_2$  layers are in parallel with the rGO plane but the size of  $\text{MoS}_2$  crystals is much smaller than the rGO nanosheets. The small 2H- $\text{MoS}_2$  crystals form a 2D powder with random rotational orientations in the rGO plane, thus giving continuous rings in SAED. The XRD, Raman spectroscopy, SEM and TEM results consistently indicate the in-plane growth of few-layer polycrystalline  $\text{MoS}_2$  nanopatches on the large monocrystalline rGO nanosheets, forming a unique  $\text{MoS}_2/\text{rGO}$  hybrid.

▪ **Materials Composition Analyses:**

XPS was used to analyze the chemical composition of the synthesized  $\text{MoS}_2/\text{rGO}$  hybrids. Figure 4 shows the Mo 3d spectra in the binding energy (B.E.) range of 222-240 eV and S 2p spectra in the B.E. range of 159-169 eV of  $\text{MoS}_2/\text{rGO}$ -600,  $\text{MoS}_2/\text{rGO}$ -325,  $\text{MoS}_2/\text{rGO}$ -250 and the  $\text{MoS}_3/\text{rGO}$  intermediate material. The S 2p spectra of  $\text{MoS}_2/\text{rGO}$ -600 consists of a pair of peaks at 162.09 eV (for  $2p_{3/2}$ ) and 163.27 eV (for  $2p_{1/2}$ ) with an intensity ratio of 2:1, attributed to  $\text{S}^{2-}$  bridging sulfur of  $\text{MoS}_2$  structure. At lower annealing temperatures of 325 °C, another small pair attributed to  $\text{S}_2^{2-}$  sulfur (blue curves in Figure 4(d)) needs to be included in the deconvolution, which appear at higher B.E. of 163.41 eV and 164.58 eV. The relative ratio of the integrated peak area of  $\text{S}_2^{2-}$  to  $\text{S}^{2-}$  increases from 0.16 in  $\text{MoS}_2/\text{rGO}$ -325 to 1.15 as the annealing temperature drops to 250 °C, indicating the increase of atomic ratio in  $\text{S}_2^{2-}$  relative to  $\text{S}^{2-}$ .

The  $\text{MoS}_3/\text{rGO}$  intermediate gives an atomic ratio of  $\text{S}_2^{2-}$  to  $\text{S}^{2-}$  at 1.17, similar to the  $\text{MoS}_2/\text{rGO}$ -250, but both  $\text{S}_2^{2-}$  and  $\text{S}^{2-}$  shift to higher BE. This is consistent with the fact that the intermediate product after microwave irradiation is dominated by amorphous  $\text{MoS}_3$  which has a linear chain-like structure with a possible composition of  $\text{Mo}^{4+}(\text{S}^{2-})(\text{S}_2^{2-})$  as refined by Hibble

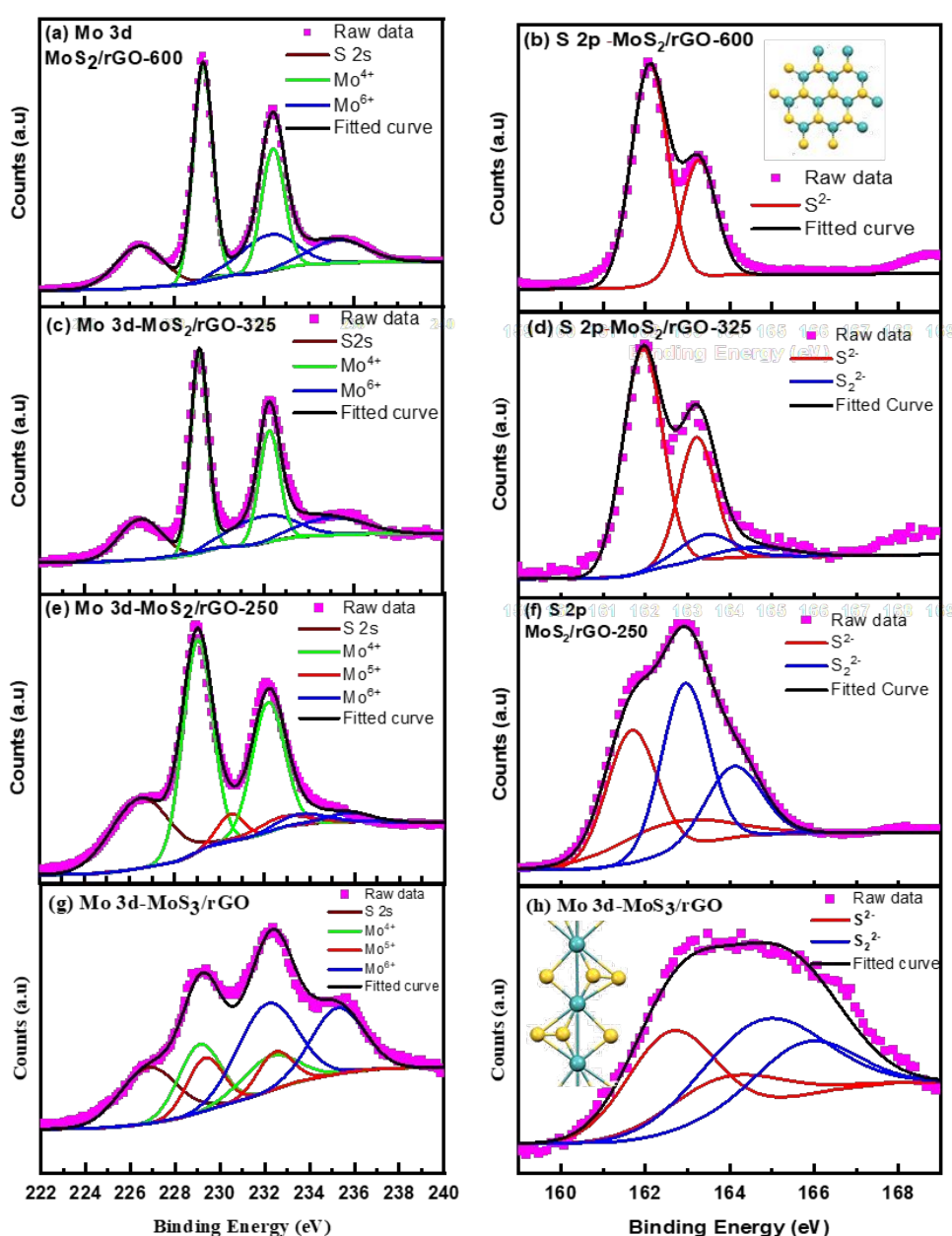


**Figure 4.** The Mo 3d and S 2p XPS spectra of (a,b)  $\text{MoS}_2/\text{rGO}$ -600, (c,d)  $\text{MoS}_2/\text{rGO}$ -325), (e,f)  $\text{MoS}_2/\text{rGO}$ -250, (g,h)  $\text{MoS}_3/\text{rGO}$ -intermediate product. The inset of panel (b) shows the schematic structure of the hexagonal  $\text{MoS}_2$  nanopatches. The inset of panel (h) shows the schematic structure of  $\text{MoS}_3$  chain.

et al.<sup>51</sup> based on the original model proposed by Liang et al.<sup>52-55</sup>. In this model, both  $\text{S}_2^{2-}$  and  $\text{S}^{2-}$

are present as bridging atoms to link the adjacent two  $\text{Mo}^{4+}$  atoms (as illustrated in the inset of Figure 4(h)).

However, the atomic ratio of  $\text{S}_2^{2-}$  to  $\text{S}^{2-}$  in both  $\text{MoS}_3/\text{rGO}$  intermediate and  $\text{MoS}_2/\text{rGO}$ -250 is lower than the ratio of 2 in pure  $\text{MoS}_3$ , indicating the presence of extra  $\text{S}^{2-}$  atoms due to partial formation of  $\text{MoS}_2$  and some unreacted ATM precursors. It is known that, in inert gas at  $\sim 1$  bar pressure, ATM thermally decomposes into  $\text{MoS}_3$  between 260 to 300 °C and is then further converted into microcrystalline  $\text{MoS}_2$ <sup>56</sup>. The high pressure ( $\sim 21$  bar) during the microwave process in this study may facilitate the partial conversion of ATM precursor into  $\text{MoS}_3$  at lower temperature ( $\sim 170$  °C), yielding a mixture of  $\text{MoS}_3$ ,  $\text{MoS}_2$  and ATM residue. During thermal annealing in  $\text{H}_2$  at 600 °C, the amorphous  $\text{MoS}_3$  chains are converted into nearly perfect  $\text{MoS}_2$  layers as shown in the inset of Figure 4 (b). At the lower annealing temperature at 250 °C, a high density of  $\text{MoS}_3$  residue is retained and presents as S-rich (or Mo-deficient) defects. This is very different from the commonly studied S-deficient defects in the  $\text{MoS}_2$  nanosheets prepared by the hydrothermal method<sup>22</sup>. Among the four samples, the atomic percentage of S in form of  $\text{S}_2^{2-}$  increases from 0% in  $\text{MoS}_2/\text{rGO}$ -600 to 13.5% in  $\text{MoS}_2/\text{rGO}$ -325, 53.5% in  $\text{MoS}_2/\text{rGO}$ -250 and 54.0% in un-annealed  $\text{MoS}_3/\text{rGO}$  intermediate.

The Mo 3d spectra of  $\text{MoS}_2/\text{rGO}$ -600 and  $\text{MoS}_2/\text{rGO}$ -325 can be nicely fit with two pairs of 3d peaks with the area ratio between  $3d_{5/2}$  and  $3d_{3/2}$  maintained as 3:2 and the splitting energy between them set as 3.13 eV. However, the Mo 3d spectrum of  $\text{MoS}_2/\text{rGO}$ -250 need to include one more pair of peaks in the curve fitting. As shown in Table S1, among these deconvoluted peaks, the B.E. of  $3d_{5/2}$  peaks at 229.28 eV, 229.12 eV and 229.03 eV in  $\text{MoS}_2/\text{rGO}$ -600,  $\text{MoS}_2/\text{rGO}$ -325 and  $\text{MoS}_2/\text{rGO}$ -250 can be attributed to the  $\text{Mo}^{4+}$  composition of  $\text{MoS}_2$  in these samples. The smaller  $3d_{5/2}$  peaks at higher B.E. around 232.18 eV, 231.90 eV and 232.68 eV can be attributed to the  $\text{Mo}^{6+}$  in either the ATM residue or  $\text{MoO}_3$  in the samples (as revealed by the Raman spectrum in Figure 2(b)). In addition to the above-mentioned two pairs of peaks,

there is a small additional pair of peaks with  $3d_{5/2}$  at around 230.52 eV, which can be attributed to  $\text{Mo}^{5+}$  in  $\text{MoS}_2/\text{rGO-250}$ . It is worth noting that the  $\text{Mo}^{4+} 3d_{5/2}$  peak slightly shifts to lower binding energy with the decreasing temperature. This correlates with the increasing  $\text{S}_2^{2-}$  percentage as the annealing temperature is reduced. The elemental ratio of Mo:S is about 1:1.9, 1:2.3 and 1:2.9 in  $\text{MoS}_2/\text{rGO-600}$ ,  $\text{MoS}_2/\text{rGO-325}$  and  $\text{MoS}_2/\text{rGO-250}$ , respectively. As a result, either a large number of molybdenum vacancies or increased sulfur contents at the edge of  $\text{MoS}_2$  nanopatches present in the low-temperature annealed samples, both of which is beneficial to  $\text{Zn}^{2+}$  ion storage. For the un-annealed  $\text{MoS}_3/\text{rGO}$  intermediate sample, both the S 2p spectrum (Figure 4(h)) and the Mo 3d spectrum (Figure 4(g)) are more complicated due to the presence of a mixture of  $\text{MoS}_3$ , ATM residue and  $\text{MoS}_2$ . The S 2s peak is also observed at the B.E. of  $\sim 226.4 - 226.9$  eV in panel (a), (c), (e) and (g) of Figure 4, which increases as the annealing temperature is decreased, consistent with the increased ratio of S 2p and Mo 3d peaks.

The composition of the hybrid materials is further analyzed with thermogravimetric analysis (TGA) from room temperature to 600 °C in the air atmosphere. Figure S8 shows the TGA curves of  $\text{MoS}_2/\text{rGO-600}$ ,  $\text{MoS}_2/\text{rGO-325}$ ,  $\text{MoS}_2/\text{rGO-250}$ ,  $\text{MoS}_3/\text{rGO}$  intermediate and two control samples (commercial  $\text{MoS}_2$  flakes and bare rGO). The  $\text{MoS}_2$  standard (blue curve) remains stable till 370 °C but shows a weight loss of 10.1% between 370 °C and 550°C due to the conversion of  $\text{MoS}_2$  to  $\text{MoO}_3$ . The bare rGO (green curve) illustrates a rapid weight loss starting from 420 °C till 563 °C by 93.36% due to oxidation of rGO into  $\text{CO}_2$ , with about 6.64% of graphitic carbon remaining up to 600 °C. The  $\text{MoS}_2/\text{rGO-600}$  (purple curve) demonstrates a weight loss of 27.34% from 370 °C till 600 °C, attributed to the concurrent effects of rGO decomposition and the conversion of  $\text{MoS}_2$  to  $\text{MoO}_3$ . The weight percentage of  $\text{MoS}_2$  in the  $\text{MoS}_2/\text{rGO-600}$  is calculated to be 79.29% and the rest 20.71% is rGO (see the description in the SI following Figure S9). This estimation is in good agreement with the XRD, Raman and

XPS analyses. The TGA curves of the other samples including MoS<sub>2</sub>/rGO-325, MoS<sub>2</sub>/rGO-250 and MoS<sub>3</sub>/rGO intermediate show a consistent trend, but the weight loss starts from the room temperature and continues up to ~560 °C. The overlap of multiple reactions of the unstable intermediate species makes it difficult to derive the accurate composition based on the stoichiometric calculations.

A combustion CHNS elemental analysis was employed to determine the more accurate weight percentage (wt%) of the elements including C, O, N, H and S, as listed in Table S3. The approximate wt% of MoS<sub>x</sub> is calculated to be 78.40%, 71.99%, 74.86% and 65.81% for MoS<sub>2</sub>/rGO-600, MoS<sub>2</sub>/rGO-325, MoS<sub>2</sub>/rGO-250 and MoS<sub>3</sub>/rGO-intermediate, respectively. The corresponding wt% of carbon in these hybrid material is 19.98%, 22.46%, 18.62% and 20.31%. It is significant to note that the wt% of oxygen is determined to be 11.07% in MoS<sub>3</sub>/rGO-intermediate and 1.17% in MoS<sub>2</sub>/rGO-600. This decrease in oxygen wt% at the higher annealing temperature can be attributed to the further reduction of rGO. It is noteworthy that it is not possible to separate the contributions of MoS<sub>3</sub>, MoS<sub>2</sub> and MoO<sub>3</sub> by these elemental analyses. Thus, to make a consistent comparison, we use the total mass of Mo compounds in the MoS<sub>x</sub>/rGO hybrid material, denoted as MoS<sub>x</sub>, in calculating the specific capacity in the following section for battery tests.

#### ▪ **Electrochemical Evaluation of Energy Storage:**

The MoS<sub>2</sub>/rGO hybrid materials are first tested as the anode in half-cells versus a Li counter electrode in the voltage range of 0.50 to 3.0 V. The low voltage limit is set at 0.50 V to avoid irreversible reduction of MoS<sub>x</sub> into Mo metal. Figure 5(a) shows the representative results from two rate-performance sequences of the MoS<sub>2</sub>/rGO-600 electrode at the current density of 145, 217, 434 and 867 mA g<sup>-1</sup> which corresponds to the approximate experimental C-rates of C/5.5, C/2.2, 1C and 2C, respectively. Figure 5(a) illustrates an impressive initial

specific discharge capacity of  $580 \text{ mAh g}_{\text{MoS}_x}^{-1}$  at  $145 \text{ mA g}^{-1}$ , which then falls rapidly to  $519 \text{ mAh g}_{\text{MoS}_x}^{-1}$  (corresponding to  $\sim 3.1 \text{ Li}^+$  ion insertion per  $\text{MoS}_2$ ) in the 10<sup>th</sup> cycle due to irreversible changes in the structure caused by the intercalation of more than one  $\text{Li}^+$  ion per  $\text{MoS}_2$ . In the meantime, the coulombic efficiency (CE) defined as the ratio of the discharge capacity to the preceding charge capacity (see Equation (2) in SI) quickly increases from 86.6% in the first cycle to 98.3% in the 5<sup>th</sup> cycle and maintains over 99.6% after the 10<sup>th</sup> cycle, indicating the good reversibility of the electrode. The electrode stability is improved after extended cycling or at higher current rates. The  $\text{MoS}_2$  nanopatches grown on the rGO template using the microwave irradiation are more uniform and homogeneous than the previously reported hydrothermal methods<sup>57</sup>. This leads to slightly higher specific capacity and better stability than the  $\text{MoS}_2$  nanosheets deposited on electrospun carbon nanofibers by Wang et al<sup>58</sup>. Other samples including  $\text{MoS}_2/\text{rGO}$ -325,  $\text{MoS}_2/\text{rGO}$ -250 and  $\text{MoS}_3/\text{rGO}$  intermediate show the similar behavior (Figure S9) but with slightly smaller specific capacity at the lower annealing temperature. However, the materials annealed at lower temperature become

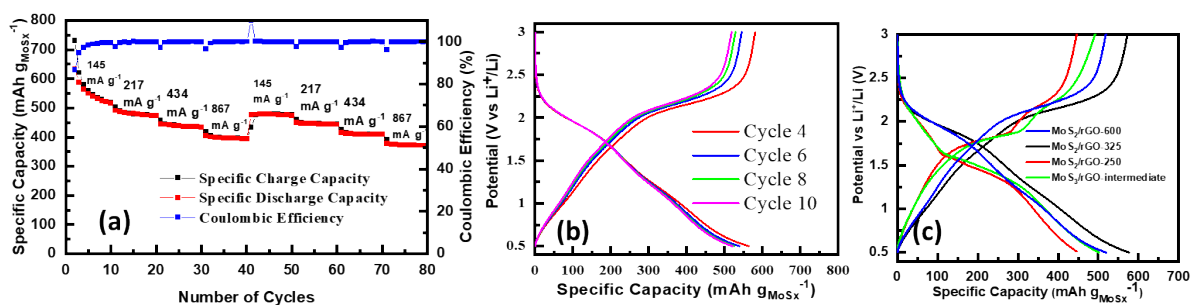


**Figure 5.** (a) The rate-performance tests of the LIB half-cell with the  $\text{MoS}_2/\text{rGO}$ -600 cathode vs. a Li disk anode at 100, 150, 300, 600 mA cell current in the cell voltage window of 0.50 – 3.0 V. (b) The galvanostatic charge/discharge curves in the initial 10 cycles at  $145 \text{ mA g}^{-1}$  ( $\sim C/4$  rate) in (a). (c) The galvanostatic charge/discharge curves of LIB half-cells made of  $\text{MoS}_2/\text{rGO}$ -600 at  $145 \text{ mA g}^{-1}$  (blue),  $\text{MoS}_2/\text{rGO}$ -325 at  $97 \text{ mA g}^{-1}$  (black),  $\text{MoS}_2/\text{rGO}$ -250 at  $160 \text{ mA g}^{-1}$  (red) and  $\text{MoS}_3/\text{rGO}$  intermediate material at  $87 \text{ mA g}^{-1}$  (green) in the 10<sup>th</sup> cycle at 100 mA cell current rate. Be noted that all measurements in panels (b) and (c) were done at 100  $\mu\text{A}$  cell current, but are translated into different current densities due to variation of mass loading on each electrode.

stabilized slightly faster in the initial cycles. The overall effect of the annealing temperature on Li-ion storage is rather small.

Lithiation in MoS<sub>2</sub> occurs via two processes including intercalation and conversion reaction. Initial lithiation process in the potential window of 1.0-3.0 V involves the intercalation of Li<sup>+</sup> ions into the interlayer spacing of MoS<sub>2</sub> resulting in the formation of intermediate Li<sub>x</sub>MoS<sub>2</sub> (0 < x ≤ 1) rendering a theoretical capacity of 167 mAh g<sup>-1</sup> (n=1) for one Li<sup>+</sup> insertion<sup>59</sup>. The conversion reaction of Li<sub>x</sub>MoS<sub>2</sub> into metallic Mo and Li<sub>2</sub>S takes place around at lower potential between 0.57 V and 0.34 V<sup>60</sup>, which gives further increased capacity up to 664 mAh g<sup>-1</sup> (corresponding to ~4 Li<sup>+</sup> ion insertion), but also causes the structural degradation and shuttle effect. In this study, we have applied a potential window of 0.5 – 3.0 V to limit the irreversible conversion of Li<sub>x</sub>MoS<sub>2</sub> into metallic molybdenum and Li<sub>2</sub>S. Thus the specific capacity is comparable to studies in the similar potential window<sup>57, 61</sup>. On the other hand, the larger interlayer spacing and the presence of defects (Mo-vacancies) in the MoS<sub>2</sub> structure facilitates intercalation of more Li<sup>+</sup> ions and thereby increases the specific capacity of the Li<sub>x</sub>MoS<sub>2</sub> phase up to x = ~3.0. The galvanostatic charge/discharge curves of MoS<sub>2</sub>/rGO-600 in the first 10 cycles in Figure 5(b) only show a few weak kinks during Li<sup>+</sup> insertion, but a clear voltage plateau is observed around 2.10 V in the extraction curves, indicating that it indeed involves Li<sup>+</sup> ion intercalation/de-intercalation between the MoS<sub>2</sub> layers. The long term stability of MoS<sub>2</sub>/rGO-600 is shown in Figure S10 with a higher initial specific capacity of 393.5 mAh g<sub>MoS<sub>x</sub></sub><sup>-1</sup> and the capacity retention of ~89.12% after 50 cycles.

Figure 5(c) further shows that the MoS<sub>2</sub>/rGO-600 and MoS<sub>2</sub>/rGO-325 electrodes behave similarly. The MoS<sub>2</sub>/rGO-250 and MoS<sub>3</sub>/rGO intermediate electrodes, however, show slightly lower specific capacity of ~446 – 492 mAh g<sub>MoS<sub>x</sub></sub><sup>-1</sup> in the 10<sup>th</sup> cycle at 100 μA. The difference in the obtained specific capacity is mainly attributed to the varied mass loadings of MoS<sub>3</sub>/rGO materials in each electrode (which translate into different current densities of ~76

to 173 mA g<sup>-1</sup>) rather than the intrinsic materials properties. All the four electrodes show substantially higher specific capacities than 167 mAh g<sub>MoS<sub>x</sub></sub><sup>-1</sup> for one Li<sup>+</sup> insertion. The rGO (with the approximate wt% of 21.15% to 31.38%) also exhibits low Li ion storage capacities (~53 – 110 mAh g<sub>rGO</sub><sup>-1</sup>) as shown in the tests with control rGO samples in Figure S11. This contribution, however, only accounts for less than 8% of the specific capacity in Figure 5 and Figure S9, as described Table S4 of the SI. The calibrated specific capacity attributed to MoS<sub>x</sub> varies from 446 to 573 mAh g<sub>MoS<sub>x</sub></sub><sup>-1</sup>, which still well exceeds the theoretical value of one Li<sup>+</sup> ion intercalation per MoS<sub>2</sub>. It corresponds to about 3 Li<sup>+</sup> insertion per MoS<sub>x</sub>. As shown in panels (a), (c), (e) and (g) of Figure S9, all four MoS<sub>x</sub>/rGO hybrids exhibit comparable capacity in the range of ~440 to 550 mAh g<sub>MoS<sub>x</sub></sub><sup>-1</sup> after returning to the lowest rate (100 μA) in the 45<sup>th</sup> cycle, indicating that the materials are stable and the Li<sup>+</sup> ion insertion/extraction is reversible.

The capability of high Li<sup>+</sup> ion insertion (~3 Li<sup>+</sup> per MoS<sub>x</sub>) can be attributed to (i) the enhanced electrical conductivity and stability provided by the rGO template and (ii) the significantly increased number of active sites due to the small MoS<sub>2</sub> nanopatches (~4.5 nm by XRD in earlier discussions) even in the 600 °C annealed MoS<sub>2</sub>/rGO hybrid. The small MoS<sub>2</sub> nanopatches seems to be the main factor for the observed high Li<sup>+</sup> storage capacity. Further introducing Mo vacancies at lower annealing temperature did not have significant effects. It is noteworthy that over 800 mAh g<sub>MoS<sub>x</sub></sub><sup>-1</sup> Li<sup>+</sup> storage capacity at the low rate (~100 mA g<sub>MoS<sub>x</sub></sub><sup>-1</sup>) has been reported by Wu et al. with S-defect rich ultrathin MoS<sub>2</sub> nanosheets<sup>61</sup> and by Chen et al. with defect-rich few-layer MoS<sub>2</sub> nanosheets on a carbon support<sup>62</sup>. While these studies support that defects in MoS<sub>2</sub> nanosheets are beneficial in enhancing Li<sup>+</sup> storage, the lower potential limit in their charge/discharge measurements was set at 0.01 V vs. Li<sup>+</sup>/Li, which unavoidably involved conversion of MoS<sub>2</sub> to Li<sub>2</sub>S. We deliberately set our lower limit at 0.50 V vs. Li<sup>+</sup>/Li to eliminate the irreversible conversion reaction. Therefore, only intercalation of Li<sup>+</sup> ions between MoS<sub>2</sub> nanopatches was measured in our study.

The MoS<sub>2</sub>/rGO hybrid materials are further assessed as the cathode in aqueous Zn-ion half-cells in the voltage range of 0.25 to 1.30 V versus a Zn anode. Aqueous zinc ion batteries (ZIBs) have been intensively studied as a suitable alternative to Lithium ion batteries (LIBs) for large-scale energy storage systems owing to the high volumetric capacity (5,854 mAh cm<sup>-3</sup>) and increased safety. MoS<sub>2</sub> has been studied as a potential host for the divalent Zn<sup>2+</sup> cations due to its unique 2D layered structure analogous to graphene and the increased interlayer distance of ~0.62 nm. The weak van der Waals forces between the layers make the intercalation of larger Na<sup>+</sup> ions (1.02 Å in radius)<sup>44, 58, 63</sup> and multivalent Zn<sup>2+</sup> ions (0.74 Å in radius)<sup>10</sup> more feasible due to the ability to accommodate the volume expansion during the intercalation process.

In contrast to Li<sup>+</sup> ion storage, the defects in the MoS<sub>x</sub>/rGO hybrid materials show a much stronger effect on the Zn<sup>2+</sup>-ion storage performance. The more defective sample MoS<sub>2</sub>/rGO-250 behaves much better than other samples. Figure 6(a) illustrates the rate performance of the defective MoS<sub>2</sub>/rGO-250 cathode. In the initial cycle, a high specific charge capacity of 336 mAh g<sub>MoS<sub>x</sub></sub><sup>-1</sup> is obtained at 104 mA g<sup>-1</sup> current rate (~C/1.8), but the CE is only 88%. The specific charge capacity rapidly drops to 196 mAh g<sub>MoS<sub>x</sub></sub><sup>-1</sup> in the 3<sup>rd</sup> cycle while the CE quickly rises to ~100% and maintains at this value in later cycles. The capacity becomes more stable after 10 cycles but drops to 130 mAh g<sub>MoS<sub>x</sub></sub><sup>-1</sup>. The stability is further improved as the current density is increased to 208 mA g<sup>-1</sup> (~2C) followed by 313 mA g<sup>-1</sup> (~4C) and 418 mA g<sup>-1</sup> (~7.5C). The CE maintains at 100%. The electrode becomes much more stable in the 2<sup>nd</sup> rate sequence starting at the 41<sup>st</sup> cycle at 104 mA g<sup>-1</sup>. The CV curves of the MoS<sub>2</sub>/rGO-250 cathode in Figure 6(b) show the continuous supercapacitor-like feature without any clear redox peaks. The corresponding charge/discharge curves in the 2<sup>nd</sup> cycles from different samples in Figure 6(c) are smooth without any voltage plateaus. Clearly, the Zn-ion storage is mostly based on surface reactions at the edges or the defect sites of the MoS<sub>2</sub> nanopatches. As a result,

the annealing temperature (and resulted defect density) has a much more dramatic effect on the Zn-ion storage capacity and stability. Comparing to MoS<sub>2</sub>/rGO-250, the specific charge capacity of the MoS<sub>2</sub>/rGO-325 cathode is only ~56 mAh g<sup>-1</sup> in the 2<sup>nd</sup> cycle and that of MoS<sub>2</sub>/rGO-600 is almost negligible (~5.8 mAh g<sup>-1</sup>), as shown in Figure 6(c).

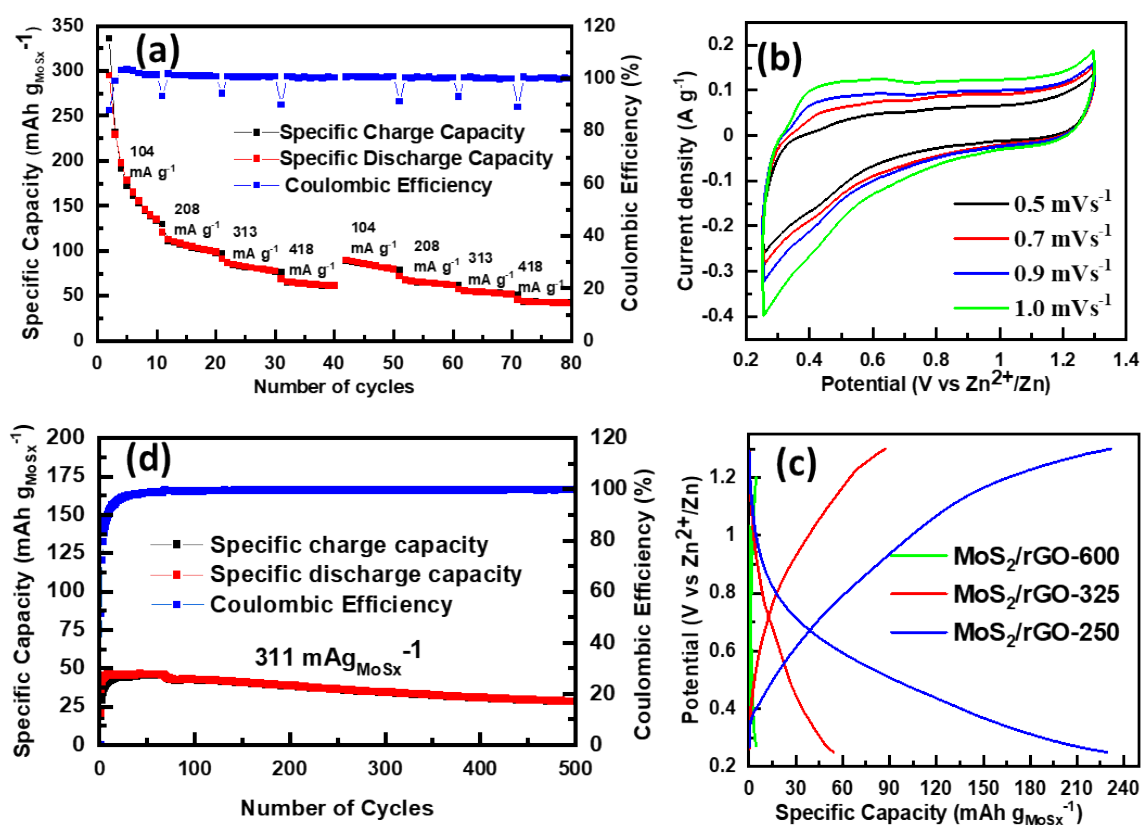


**Figure 6.** (a) Rate performance of MoS<sub>2</sub>/rGO-250 in a Zn-ion battery half-cell at 100, 200, 300 and 400 mA cell currents, which are converted to corresponding current densities for ease of comparison among different cells. (b) CV curves of MoS<sub>2</sub>/rGO-250 at various scan rates in the cell voltage window of 0.25 – 1.30 V (vs. Zn<sup>2+</sup>/Zn). (c) Galvanostatic charge-discharge curves in the 2<sup>nd</sup> cycle of Zn-ion battery half-cells at 78 mA g<sup>-1</sup> with MoS<sub>2</sub>/rGO-600, MoS<sub>2</sub>/rGO-325 and MoS<sub>2</sub>/rGO-250 cathode, respectively. (d) Long-term stability of a Zn-ion half-cell with the MoS<sub>2</sub>/rGO-250 cathode at the charge/discharge current density of 311 mA g<sup>-1</sup>.

As shown in Figure S12, MoS<sub>2</sub>/rGO-600 and MoS<sub>2</sub>/rGO-325 not only show lower capacities, but also lower CEs than MoS<sub>2</sub>/rGO-250. In contrast, the un-annealed MoS<sub>3</sub>/rGO intermediate sample shows the similar behavior as MoS<sub>2</sub>/rGO-250 and remains stable over 100

cycles (Figures S13 (b)) at 200  $\mu\text{A}$  current rate ( $\sim 345 \text{ mA g}^{-1}$ ). But  $\text{MoS}_2/\text{rGO-250}$  shows higher capacity than the  $\text{MoS}_3/\text{rGO}$  intermediate, i.e.  $\sim 336$  to  $130 \text{ mAh g}_{\text{MoS}_x}^{-1}$  in the first 10 cycles at  $104 \text{ mA g}^{-1}$  in Fig. 6(a) vs.  $\sim 152$  to  $58 \text{ mAh g}_{\text{MoS}_x}^{-1}$  at  $75 \text{ mA g}^{-1}$  in Figure S12(g). This confirms that the major Zn-ion storage host is the defective  $\text{MoS}_2$  rather than  $\text{MoS}_3$  intermediate (or ATM residue). The stability of  $\text{MoS}_2/\text{rGO-250}$  cathode is further demonstrated in long cycling results in Figure 6(d). The capacity at the  $311 \text{ mA g}^{-1}$  current rate ( $\sim 7.5\text{C}$ ) only drops by  $\sim 38\%$  from the highest value of  $\sim 45 \text{ mAh g}_{\text{MoS}_x}^{-1}$  at the initial cycles to  $\sim 29 \text{ mAh g}_{\text{MoS}_x}^{-1}$  at the 500<sup>th</sup> cycle. In contrast to Li-ion storage, the contribution of rGO to  $\text{Zn}^{2+}$  ion storage is only  $\sim 1.5$  to  $4 \text{ mAh g}_{\text{rGO}}^{-1}$  (as shown in Figure S14), which is negligible.

It is interesting that the small  $\text{MoS}_2$  nanopatches in the  $\text{MoS}_2/\text{rGO}$  hybrids seems to be sufficient to provide enhanced  $\text{Li}^+$  ion intercalation and give high Li-ion storage capacity ( $\sim 3 \text{ Li}^+$  per  $\text{MoS}_2$ ). Adding further defect density in the  $\text{MoS}_2/\text{rGO}$  samples has much smaller effects on the Li-ion storage. In contrast, the highly defective  $\text{MoS}_2/\text{rGO-250}$  sample prepared by annealing at  $250 \text{ }^\circ\text{C}$  performs much better in Zn-ion storage than the less defective  $\text{MoS}_2/\text{rGO-600}$  sample, with a very high initial capacity of  $\sim 300 \text{ mAh g}_{\text{MoS}_x}^{-1}$  at the low current density but fades quickly. The Zn-ion storage seems to be mainly based on pseudocapacitive surface reactions at the edge or defect sites of the  $\text{MoS}_2$  nanopatches. Overall, the stability and CE are lower at low current rates, particularly for Zn-ion storage. But they can be dramatically improved at higher current rates. The high CE and reversible  $\text{Zn}^{2+}$  ion storage can be obtained in the defective  $\text{MoS}_2/\text{rGO-250}$  sample, which may be attributed to the increased defect density and terminal  $\text{S}_2^{2-}$  edges, as revealed by the XPS analysis. The produced small  $\text{MoS}_2$  nanopatches are favorable for  $\text{Zn}^{2+}$  adsorption and fast surface reactions. The ability to increase  $\text{Zn}^{2+}$  ion storage by introducing more defects in  $\text{MoS}_2$  is consistent with the study by Xu et al.<sup>22</sup> Our stabilized specific capacity with the  $\text{MoS}_2/\text{rGO-250}$  sample ( $\sim 128 \text{ mAh g}_{\text{MoS}_x}^{-1}$  at  $\sim 104 \text{ mA g}^{-1}$  after 10 cycles) is comparable to that by Xu et al. ( $\sim 110 \text{ mAh g}^{-1}$  at  $\sim 200 \text{ mA g}^{-1}$ )<sup>22</sup>.

However, the nature of the defects is very different. The S-rich defects in MoS<sub>2</sub>/rGO-250 in this study (with a S:Mo ratio of ~2.9:1) likely present larger electrostatic interactions with the divalent Zn<sup>2+</sup> cations than that in the S-deficient MoS<sub>2</sub> (with a S:Mo ratio of 1.5:1) by Xu et al.<sup>22</sup>. This may cause irreversible structural changes during insertion of large amount of Zn<sup>2+</sup> ions in MoS<sub>2</sub>/rGO-250. At high current rates, there is less intercalation into the MoS<sub>2</sub> layers and thus the performance is dominated by fast surface reactions at the edges and defect sites, making it much more stable. It is interesting that all MoS<sub>2</sub>/rGO hybrid materials are much more stable in intercalation/deintercalation of smaller Li<sup>+</sup> ions. Further study to find a way to maintain the high Zn-ion storage capacity of the defective MoS<sub>2</sub>/rGO-250 hybrid as shown in the initial cycles would be important in ZIB development.

### **Conclusion:**

In summary, a set of MoS<sub>2</sub>/rGO hybrid materials were prepared by applying the microwave specific heating on graphene oxide and molecular Mo precursors followed by the thermal annealing in 3% H<sub>2</sub> and 97% Ar at different temperature. The microwave process was able to convert graphene oxide to ordered rGO nanosheets, which were sandwiched with uniform thin layers of intermediate materials dominated by amorphous MoS<sub>3</sub>. The thermal annealing process converted the amorphous MoS<sub>3</sub> layers into 2D MoS<sub>2</sub> nanopatches, whose defect density can be tuned by controlling the annealing temperature at 250, 325 and 600 °C. The MoS<sub>2</sub>/rGO sample annealed at 600 °C was found to consist of 2D nanopatches of MoS<sub>2</sub> crystals (~ 4.5 nm in size) randomly oriented on monocrystalline reduced graphene surface while the samples annealed at 250 and 325 °C showed a S to Mo ratio larger than 2:1, indicating the presence of high-density S-rich or Mo-deficient defects which are different from the S-deficient defects by hydrothermal synthesis in literature. All three MoS<sub>2</sub>/rGO samples and the MoS<sub>3</sub>/rGO intermediate showed high Li-ion intercalation capacities in initial cycles (over ~519

mAh  $\text{g}_{\text{MoS}_x}^{-1}$ ,  $\sim 3.1$   $\text{Li}^+$  ions per  $\text{MoS}_2$ ). The small  $\text{MoS}_2$  nanopatches in the  $\text{MoS}_2/\text{rGO}$  samples seemed to be more important for Li-ion storage while the effect of the additional S-rich defects in  $\text{MoS}_2$  was found insignificant. In contrast, the Zn-ion storage properties strongly depended on the S-rich defects in the sample. The highly defective  $\text{MoS}_2/\text{rGO}$  sample prepared by annealing at  $250^\circ\text{C}$  provided the highest initial Zn-ion storage capacity ( $\sim 300$  mAh  $\text{g}_{\text{MoS}_x}^{-1}$ ) and nearly 100% coulombic efficiency, which was dominated by pseudocapacitive behavior based on surface reactions at the edges or defects in the  $\text{MoS}_2$  nanopatches. Even though significant fading in specific capacity occurred at the initial cycles at low current densities, stable charge/discharge can be obtained at higher charge/discharge current densities or after extended cycles. This study validates that defect engineering is critical in the divalent Zn-ion storage.

#### **Author Contributions:**

Kamalambika Muthukumar: Conceptualization, data acquisition, formal analysis, investigation, writing – original draft and writing – review & editing. Levon Leban II: partial data acquisition, formal analysis. Archana Sekar: Partial data acquisition, formal analysis, writing – review & editing. Ayyappan Elangovan: Partial data acquisition. Nandini Sarkar: Partial data acquisition. Jun Li: Funding acquisition, conceptualization, investigation, project administration, supervision, visualization, methodology, writing – original draft and writing – review & editing.

#### **Conflict of interest:**

There are no conflicts to declare.

## Acknowledgements:

This work is supported by the National Science Foundation grant DMR-1707585. We would like to thank Dr. Dan Boyle at Kansas State University's microscopy facility for help in TEM measurements and Prof. Christer Aakeroy at Kansas State University for support in TGA measurements. We wish to thank ISU Chemical Instrumentation Facility staff member, Dr. Sarah Cady for assistance pertaining to the PE 2100 CHN/S elemental analysis results included in this publication. The XPS characterization was performed in the Nebraska Nanoscale Facility: National Nanotechnology Coordinated Infrastructure and the Nebraska Center for Materials and Nanoscience, which are supported by the National Science Foundation under Award ECCS: 2025298 and the Nebraska Research Initiative.

## References

1. F. Díaz-González, A. Sumper, O. Gomis-Bellmunt and R. Villafáfila-Robles, *Renewable and Sustainable Energy Reviews* 2012, **16**, 2154-2171.
2. H. D. Yoo, E. Markevich, G. Salitra, D. Sharon and D. Aurbach, *Materials Today*, 2014, **17**, 110-121.
3. P. Canepa, G. Sai Gautam, D. C. Hannah, R. Malik, M. Liu, K. G. Gallagher, K. A. Persson and G. Ceder, *Chemical Reviews*, 2017, **117**, 4287-4341.
4. M. S. Whittingham, C. Siu and J. Ding, *Accounts of Chemical Research*, 2018, **51**, 258-264.
5. Y. Liang, H. Dong, D. Aurbach and Y. Yao, *Nature Energy*, 2020, DOI: 10.1038/s41560-020-0655-0.
6. A. Konarov, N. Voronina, J. H. Jo, Z. Bakenov, Y.-K. Sun and S.-T. Myung, *ACS Energy Letters*, 2018, **3**, 2620-2640.
7. K. W. Nam, H. Kim, J. H. Choi and J. W. Choi, *Energy & Environmental Science*, 2019, **12**, 1999-2009.
8. M. H. Alfaruqi, S. Islam, J. Gim, J. Song, S. Kim, D. T. Pham, J. Jo, Z. Xiu, V. Mathew and J. Kim, *Chemical Physics Letters*, 2016, **650**, 64-68.
9. Y. Li, Z. Huang, P. K. Kalambate, Y. Zhong, Z. Huang, M. Xie, Y. Shen and Y. Huang, *Nano Energy*, 2019, **60**, 752-759.
10. H. Qin, L. Chen, L. Wang, X. Chen and Z. Yang, *Electrochimica Acta*, 2019, **306**, 307-316.
11. B. Wang, Y. Han, X. Wang, N. Bahlawane, H. Pan, M. Yan and Y. Jiang, *Science*, 2018, **3**, 110-133.
12. W. J. Li, C. Han, G. Cheng, S. L. Chou, H. K. Liu and S. X. Dou, *Small*, 2019, **15**, 1900470.

13. G. Li, Z. Yang, Y. Jiang, C. Jin, W. Huang, X. Ding and Y. Huang, *Nano Energy*, 2016, **25**, 211-217.
14. W. Xu, K. Zhao and Y. Wang, *Energy Storage Materials*, 2018, **15**, 374-379.
15. P. He, Y. Quan, X. Xu, M. Yan, W. Yang, Q. An, L. He and L. Mai, *Small*, 2017, **13**, 1702551.
16. H. Li, Q. Yang, F. Mo, G. Liang, Z. Liu, Z. Tang, L. Ma, J. Liu, Z. Shi and C. Zhi, *Energy Storage Materials*, 2019, **19**, 94-101.
17. J. Liu, P. Xu, J. Liang, H. Liu, W. Peng, Y. Li, F. Zhang and X. Fan, *Chemical Engineering Journal*, 2020, **389**, 124405.
18. V. An, F. Bozheyev, F. Richecoeur and Y. Irtegov, *Materials Letters*, 2011, **65**, 2381-2383.
19. F. Bozheyev, A. Zhexembekova, S. Zhumagali, A. Molkenova and Z. Bakenov, *Materials Today: Proceedings*, 2017, **4**, 4567-4571.
20. K. Chang and W. Chen, *Chemical Communications*, 2011, **47**, 4252-4254.
21. H. S. S. R. Matte, U. Maitra, P. Kumar, B. Govinda Rao, K. Pramoda and C. N. R. Rao, *Zeitschrift für anorganische und allgemeine Chemie*, 2012, **638**, 2617-2624.
22. W. Xu, C. Sun, K. Zhao, X. Cheng, S. Rawal, Y. Xu and Y. Wang, *Energy Storage Materials*, 2019, **16**, 527-534.
23. Z. Hu, L. Wang, K. Zhang, J. Wang, F. Cheng, Z. Tao and J. Chen, *Angewandte Chemie International Edition*, 2014, **53**, 12794-12798.
24. Y. You, Y. Ye, M. Wei, W. Sun, Q. Tang, J. Zhang, X. Chen, H. Li and J. Xu, *Chemical Engineering Journal*, 2019, **355**, 671-678.
25. J. Zhou, H. Xiao, B. Zhou, F. Huang, S. Zhou, W. Xiao and D. Wang, *Applied Surface Science*, 2015, **358**, 152-158.
26. G. Barik and S. Pal, *The Journal of Physical Chemistry C*, 2019, **123**, 21852-21865.
27. Y. Li, R. Zhang, W. Zhou, X. Wu, H. Zhang and J. Zhang, *ACS Nano*, 2019, **13**, 5533-5540.
28. S. Xu, G. Zhong, C. Chen, M. Zhou, D. J. Kline, R. J. Jacob, H. Xie, S. He, Z. Huang, J. Dai, A. H. Brozena, R. Shahbazian-Yassar, M. R. Zachariah, S. M. Anlage and L. Hu, *Matter*, 2019, **1**, 759-769.
29. Y. Song, H. Rong, Y. Li, W. Liu and X. Zhang, *Journal of Materials Science*, 2020, **55**, 13871-13880.
30. B. L. Hayes, *Aldrichim. Acta*, 2004, **37**, 66-76.
31. D. Bandyopadhyay and B. K. Banik, in *Green Synthetic Approaches for Biologically Relevant Heterocycles*, ed. G. Brahmachari, Elsevier, Boston, 2015, DOI: <https://doi.org/10.1016/B978-0-12-800070-0.00019-0>, pp. 517-557.
32. T. P. Prasad, E. Diemann and A. Müller, *Journal of Inorganic and Nuclear Chemistry*, 1973, **35**, 1895-1904.
33. J. L. Brito, M. Ilija and P. Hernández, *Thermochimica Acta*, 1995, **256**, 325-338.
34. H. J. Kitchen, S. R. Vallance, J. L. Kennedy, N. Tapia-Ruiz, L. Carassiti, A. Harrison, A. G. Whittaker, T. D. Drysdale, S. W. Kingman and D. H. Gregory, *Chem Rev*, 2014, **114**, 1170-1206.
35. Y.-J. Zhu and F. Chen, *Chemical Reviews*, 2014, **114**, 6462-6555.
36. B. Wen, X. X. Wang, W. Q. Cao, H. L. Shi, M. M. Lu, G. Wang, H. B. Jin, W. Z. Wang, J. Yuan and M. S. Cao, *Nanoscale*, 2014, **6**, 5754-5761.
37. X. Zhang, D. Hayward and D. M. Mingos, *Catalysis Letters*, 2002, **84**.
38. C. O. Kappe, *Angewandte Chemie International Edition*, 2004, **43**, 6250-6284.
39. C. Sole, N. E. Drewett and L. J. Hardwick, *Faraday Discussions*, 2014, **172**, 223-237.
40. L. Bokobza, J.-L. Bruneel and M. Couzi, *Vibrational Spectroscopy*, 2014, **74**, 57-63.

41. H. Wang, J. T. Robinson, X. Li and H. Dai, *Journal Of The American Chemical Society*, 2009, **131**, 9910-9911.
42. P. Cui, J. Lee, E. Hwang and H. Lee, *Chemical Communications*, 2011, **47**, 12370-12372.
43. H. Kumar, S. Woltornist and D. Adamson, *Carbon*, 2016, **98**, 491–495.
44. E. Brown, P. Yan, H. Tekik, A. Elangovan, J. Wang, D. Lin and J. Li, *Materials & Design*, 2019, **170**, 107689.
45. P. A. Bertrand, *Physical Review B*, 1991, **44**, 5745-5749.
46. C. Lee, H. Yan, L. E. Brus, T. F. Heinz, J. Hone and S. Ryu, *ACS Nano*, 2010, **4**, 2695-2700.
47. W. Qin, T. Chen, L. Pan, L. Niu, B. Hu, D. Li, J. Li and Z. Sun, *Electrochimica Acta*, 2015, **153**, 55-61.
48. L. Liang and V. Meunier, *Nanoscale*, 2014, **6**, 5394-5401.
49. D. Kong, H. Wang, J. J. Cha, M. Pasta, K. J. Koski, J. Yao and Y. Cui, *Nano Letters*, 2013, **13**, 1341-1347.
50. S. Santha kumar, R. Cherian, A. Cheruvathor Poullose, T. Maekawa, D. Sakthikumar and P. Mohanan, *Journal of Applied Chemical Science International*, 2015, **5**, 1-11.
51. S. J. Hibble and G. B. Wood, *Journal of the American Chemical Society*, 2004, **126**, 959-965.
52. K. S. Liang, S. P. Cramer, D. C. Johnston, C. H. Chang, A. J. Jacobson, J. P. deNeufville and R. R. Chianelli, *Journal of Non-Crystalline Solids*, 1980, **42**, 345-356.
53. K. S. Liang, J. P. deNeufville, A. J. Jacobson, R. R. Chianelli and F. Betts, *Journal of Non-Crystalline Solids*, 1980, **35-36**, 1249-1254.
54. S. P. Cramer, K. S. Liang, A. J. Jacobson, C. H. Chang and R. R. Chianelli, *Inorganic Chemistry*, 1984, **23**, 1215-1221.
55. F. Z. Chien, S. C. Moss, K. S. Liang and R. R. Chianelli, *Physical Review B*, 1984, **29**, 4606-4615.
56. T. Weber, J. C. Muijsers and J. W. Niemantsverdriet, *The Journal of Physical Chemistry*, 1995, **99**, 9194-9200.
57. M. Choi, J. Hwang, H. Setiadi, W. Chang and J. Kim, *The Journal of Supercritical Fluids*, 2017, **127**, 81-89.
58. J. Wang, C. Luo, T. Gao, A. Langrock, A. C. Mignerey and C. Wang, *Small*, 2015, **11**, 473-481.
59. A. K. Budumuru, B. Rakesh and C. Sudakar, *Nanoscale*, 2019, **11**, 8882-8897.
60. Z. Zhu, Y. Tang, W. R. Leow, H. Xia, Z. Lv, J. Wei, X. Ge, S. Cao, Y. Zhang, W. Zhang, H. Zhang, S. Xi, Y. Du and X. Chen, *Angewandte Chemie International Edition*, 2019, **58**, 3521-3526.
61. Z. Wu, B. Li, Y. Xue, J. Li, Y. Zhang and F. Gao, *Journal of Materials Chemistry A*, 2015, **3**, 19445-19454.
62. B. Chen, H. Lu, N. Zhao, C. Shi, E. Liu, C. He and L. Ma, *Journal of Power Sources*, 2018, **387**, 16-23.
63. G. S. Bang, K. W. Nam, J. Y. Kim, J. Shin, J. W. Choi and S.-Y. Choi, *ACS applied materials & interfaces*, 2014, **6**, 7084-7089.